MIT Libraries | DSpace@MIT

MIT Open Access Articles

Bright and photostable single-photon emitter in silicon carbide

Massachusetts Institute of Technology

Bright and stable visible-spectrum single photon emitter in silicon carbide

Benjamin Lienhard,[1,2,*] Tim Schröder,[1] Sara Mouradian,[1] Florian Dolde,[1] Toan Trong Tran,[3] Igor Aharonovich,[3] and Dirk Englund[1]

[1]*Department of Electrical Engineering and Computer Science, Massachusetts Institute of Technology, Cambridge, MA 02139, USA*

[2]*Department of Information Technology and Electrical Engineering, ETH Zürich, Gloriastrasse 35, CH-8092 Zürich, Switzerland*

[3]*School of Mathematical and Physical Sciences, University of Technology Sydney, Ultimo, NSW 2007, Australia*

(Dated: March 21, 2016)

Abstract

Single photon sources are of paramount importance in quantum communication, quantum computation, and quantum metrology. In particular, there is great interest to realize scalable solid state platforms that can emit triggered photons on demand to achieve scalable nanophotonic networks. We report on a visible-spectrum single photon emitter in 4H-silicon carbide (SiC). The emitter is photostable at room- and low-temperature enabling photon counts per second (cps) in excess of 2×10^6 from unpatterned, bulk SiC. It exists in two orthogonally polarized states, which have parallel absorption and emission dipole orientations. Low temperature measurements reveal a narrow zero phonon line (linewidth < 0.1 nm) that accounts for > 30 % of the total photoluminescence spectrum.

INTRODUCTION

Efficient, on-demand, and robust single photon emitters (SPEs) are of central importance to many areas of quantum information processing [1]. Color centers in high-bandgap semiconductors have emerged as excellent SPEs [2, 3] that can operate even at room temperature. These include atomic defects in diamond [4], zinc oxide [5], and single rare earth ions [6] in garnets. Color centers in silicon carbide (SiC) and diamond provide optical access to internal spin states [7, 8], which can be used as quantum memories for quantum computing [9], quantum-enhanced sensing, and other quantum technologies [10, 11].

SiC is a technologically important material that is widely used in optoelectronics, high power electronics, and microelectromechanical systems [12]. It is commercially available in up to 6-inch wafers, and processes for device engineering are well developed [13]. Recently, many SPEs were reported in SiC, which were attributed to the carbon antisite-vacancy pair [14], silicon vacancies [8, 15, 16], and di-vacancies [17–19].

Here, we report on an exceptionally photostable and bright SPE in the hexagonal (4H) SiC polytype with a photoluminescence (PL) in the visible spectrum. Despite the high index of SiC (2.65 at 600 nm [20]) and the associated total internal reflection, we measure a saturated photon count rate of up to 2×10^6 cps from individual emitters, representing the brightest SPE from an unpatterned bulk semiconductor, to our knowledge. The emitter is exceptionally photostable: we observe no blinking at time scales between 100 μs to minutes, and no degradation in the PL properties after months of imaging the same emitter.

EXPERIMENTS AND RESULTS

For our experiments, we use a semi-insulating high purity (resistivity of more than 100 kΩcm) single crystal 4H-SiC 3" wafer with a thickness of 350 μm (W4TRE0R-0200, CREE, Inc). The top surface is the $\{0001\} \pm 0.25°$ crystal plane. Fig. 1(a) shows the 4H SiC lattice structure, which is characterized by sequential layers ABCB, where (A,B,C) denote the SiC bilayer structures, composed of 3 atoms connected by two bonds (Si-C-Si), that form the basis of any SiC polytype. Layers A and B differ only in a lattice shift whereas layer C describes a lattice twist by 60°.

The sample was annealed in forming gas (H$_2$:N $\rightarrow$ 1:19) at ambient pressure at 600°C.
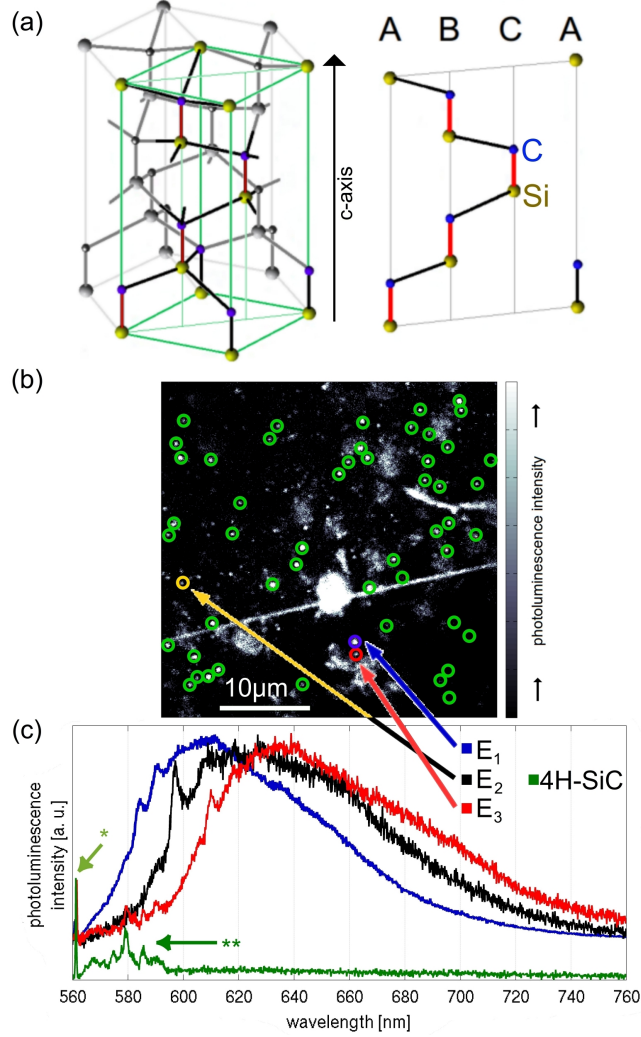
FIG. 1. (a) Three-dimensional 4H-SiC crystal lattice (carbon (C): blue, silicon (Si): yellow) in a hexagonal geometry with one green highlighted rectangular prism containing one 2 dimensional layer in its vertical diagonal plane. This plane is shown on the right hand side to illustrate the 1 dimensional lines A, B, and C. The characteristic sequential bilayers in 4H-SiC are ABCB. (b) The confocal fluorescence scan of the top surface of 4H-SiC shows a high density of bright emitters (green circles), which were separately confirmed to have single photon emission characteristics (see Fig. 2). The green bar indicates a length of 10 μm. (c) Spectra from the three characteristic 4H-SiC emitters (E_1: blue, E_2: black (yellow (b)), E_3: red) indicated in (b) representing the PL distribution over an energy range of 100 meV. The green spectra, PL of 4H-SiC, shows the characteristic first-order longitudinal optical Raman mode (labeled in the spectrum as $\star$) and the second-order Raman modes (labeled as $\star\star$).

Irradiating the sample with electrons (density: 10^{17} e$^-$cm^{-2}, energy: 10 MeV) before annealing increased the emitter density by $\sim 2\times$.

Photoluminescence at Room Temperature

After the annealing step, scanning confocal microscopy revealed individual color centers emitting in a broad spectrum covering $\sim 580 - 700$ nm, as shown in Fig. 1(b,c) under laser excitation (532 nm, 0.5 mW on sample) with a 560 nm long-pass filter. The PL was collected with a 0.9 NA microscope objective (Nikon) and detected on avalanche photo diodes (APD) via single mode fibers. Antibunched photon emission was confirmed by Hanbury Brown Twiss interferometry, as described below. Our measurements showed no evidence of blinking at time scales from 100 μs to several minutes, and the emission is stable for hours under continuous laser excitation.

The room-temperature PL spectra extend from $\sim 590 - 700$ nm ($\sim 1.77 - 2.1$ eV), with energy shifts up to ± 50 meV between different emitters. This can be seen from Fig. 1(c), which plots the individually normalized PL spectra of the three characteristic emitters E_1, E_2, E_3 labeled in Fig. 1(b). The small PL peaks between $\sim 580 - 590$ nm are also visible in the background spectrum, shown in the green curve in Fig. 1(c), and are ascribed to second-order Raman shifts [21] (Supplement 1).

We attribute the peaks at 584.8 nm (E_1), 597.3 nm (E_2), and 609.6 nm (E_3), as the room-temperature ZPLs of these emitters, though the assignment is less clear for E_1 because of the proximity to the Raman peaks.

Level System

For a better understanding of internal electron dynamics and the level structure, we measured the photon statistics of the emitter with a Hanbury Brown Twiss (HBT) interferometer. These measurements will focus on the blue shifted emitter, E_1, and the red shifted emitter, E_3, as exemplary of the broad emitter distribution. Figs. 2(a,b) show the normalized second-order autocorrelation histograms ($g^{(2)}(\tau)$, Eq. 2) without background correction, which confirm that the emission is dominated by a single emitter ($g^{(2)}(0) < 0.5$). The insets show a magnified region near $\tau = 0$. These histograms indicate a strong bunching for E_3,
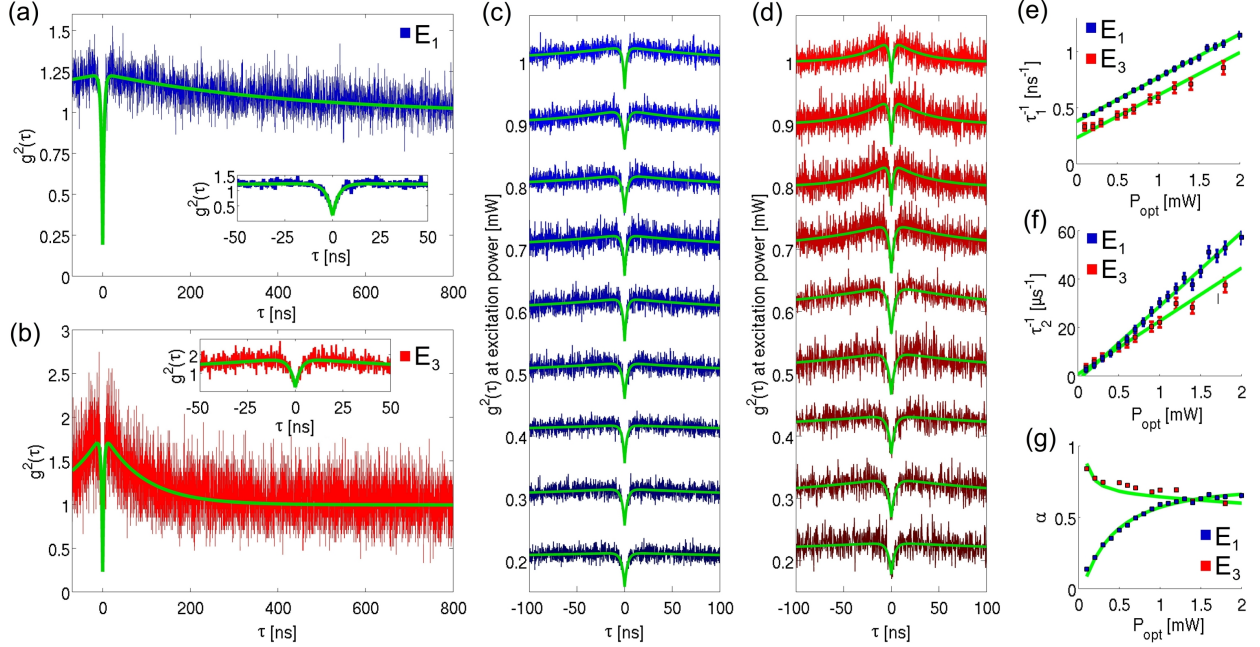
4

FIG. 2. (a,b) Second-order autocorrelation histograms of E_1 (a) and E_3 (b). (c,d) Power dependent second-order autocorrelation histograms of E_1 (c) and E_3 (d). (e,f) Reciprocal values of fitting parameters (τ_1: e, τ_2: f) for the second-order autocorrelation fit (Eq. 2). The power dependent reciprocal values of τ_1 and τ_2 are subsequently linearly fitted (green) and reflect the decay rate of the excited and metastable state at the crossover of the extrapolated linear fit with the reciprocal time axis. (g) Power dependent fitting parameter α accounting for the non-radiative transitions via the metastable state in comparison with the in Supplement 1 calculated value (green). (e-g) Error bars are representing the standard deviation calculated from the covariance matrix of each fitting routine.

but only a weak bunching for E_1. These photon bunching features suggest the presence of a dark metastable state, as analyzed below.

We use rate equation analysis to model these autocorrelation measurements. A 2-level model cannot capture the bunching behavior near $\tau = 0$. A 3-level model with pump-power dependent transition rates does capture the essential features of the second-order autocorrelation histograms, as seen in the green-curve fits in Fig. 2(a,b). This 3-level model allows direct comparison with other well-studied emitters, such as the nitrogen-vacancy (NV) center in diamond [22] and the carbon antisite-vacancy pair in SiC [14].

The 3-level system considered here consists of ground ($|g\rangle$), excited ($|e\rangle$), and metastable

($|m\rangle$) states, as illustrated in Fig. 3(a). These states are coupled by the transition rates labeled in Fig. 3(a) and mathematically described by Eq. 1:

$$\begin{pmatrix} \dot{p}_g \\ \dot{p}_e \\ \dot{p}_m \end{pmatrix} = \begin{pmatrix} -\gamma_{ge} & \gamma_{eg} & \gamma_{mg} \\ \gamma_{ge} & -\gamma_{eg} - \gamma_{em} & 0 \\ 0 & \gamma_{em} & -\gamma_{mg} \end{pmatrix} \begin{pmatrix} p_g \\ p_e \\ p_m \end{pmatrix}. \tag{1}$$

Eq. 1 describes a typical 3-level system with the transition rates (γ_{ij} between different levels $i, j \, \epsilon \, (g, e, m)$ with time dependent populations p_i) [23]. Electronic transitions in Fig. 3(a) account for contributions from excitation (γ_{ge}), radiative (γ_{eg}), as well as non-radiative decays (γ_{em}, γ_{mg}). The transitions from the ground state to the metastable state ($|g\rangle \rightarrow |m\rangle$: $\gamma_{gm} \approx 0$) and from the metastable state to the excited state ($|m\rangle \rightarrow |e\rangle$: $\gamma_{me} \approx 0$) are assumed to be insignificant and are therefore neglected.

Calculations in Supplement 1 of the decay ratio, radiative and non-radiative decays, reveal that more than 90 % of all decays are radiative. Assuming that the transition rate between $|g\rangle$ and $|e\rangle$ is significantly more dominant than the decay rate from $|e\rangle$ and $|m\rangle$ ($\gamma_{eg} \gg \gamma_{em}$), which is supported by the calculations in Supplement 1, $g^{(2)}(\tau)$ for a 3-level system can be expressed in a first order approximation as $g^{(2)}(\tau) = \lim_{t \to \infty} p_e(\tau)/p_e(t)$ [24–26].

Evaluation of the latter approximation of $g^{(2)}(\tau)$ using Eq. 1 and the initial condition of the occupation of the ground state ($p_g(0) = 1$) results in Eq. 2 with fitting parameters: τ_1, τ_2, and α.

$$g^2(\tau) \approx 1 - (1 + \alpha) \exp(-\frac{\tau}{\tau_1}) + \alpha \exp(-\frac{\tau}{\tau_2}). \tag{2}$$

Fitting parameter τ_1 describes an approximated 2-level system considering transitions between the ground and excited state. Assuming a single excited state, τ_1 can be linearly approximated as indicated in Fig. 2(e). At zero optical excitation power ($P_{opt} = 0$), τ_1 can be considered as the lifetime of the excited state [24, 26]. The linear fit in Fig. 2(e) yields a lifetime for E_1 (E_3) of about 3.33 ±0.2 ns (4.4 ±0.3 ns).

The second fitting parameter, τ_2, reflects the behavior of the metastable state. The fit in Fig. 2(f) reveals a lifetime, $\tau_2(0)$, of the metastable state of 675 ±100 ns (900 ±200 ns) for E_1 (E_3).

The third parameter of Eq. 2, α, plotted in Fig. 2(g) for E_1 and E_3, represents a fitting parameter to account for the non-radiative transitions via the metastable state and required

6

for derivation of the emitters rate equations in Supplement 1.

Additional fluorescence lifetime measurements support the 3-level model. Under pulsed excitation an excited state will decay exponentially ($I(t) = \exp{(-t/\tau)}$). A single exponential equation fits the decay rate of one single state with a time-dependent PL intensity term, $I(t)$, and with a fitting parameter τ which represents the lifetime of the spectrally detectable excited state. Fig. 3(b) shows the excited state lifetime measurement (wavelength: 532 nm, pulse length: 1 ns, frequency: 40 MHz). The optimized single-exponential fit indicates that there is only one excited state with a lifetime of 3.45 $\pm$0.1 ns for E_1 and 4.65 $\pm$0.3 ns for E_3. The measured lifetimes differ with the obtained fitting of τ_1 and τ_2 of the power dependent $g^2(\tau)$, shown in Fig. 2(e), by only 0.2 ns well within the error, supporting that a 3-level system is a suitable model for the investigated emitters.

Photoluminescence Intensity

We studied the polarization absorption and emission properties by exciting the emitters with linearly polarized light. Fig. 3(c) shows a polar plot of the excitation polarization-dependent PL intensity (without background subtraction) of E_1 fitted with a quadratic sinusoidal fit function, $\sin^2(\theta + \phi)$ consisting of an angular parameter θ, representing the rotation of the linear polarization of the pump laser, and ϕ, the orientation of the emitter, relative to an arbitrary axis. The histogram in Fig. 4(b) summarizes these polarization measurements repeated for more than 20 emitters, which reveals only two linear polarization states defined as $\phi_1 = 45°$ and $\phi_2 = 135°$.

A comparison between the obtained count rates with parallel and orthogonal, linear laser excitation relative to the emitter polarization, hence the minimum and maximum count rates in the polar plot in Fig. 3(c), reveals that all emitters are almost perfectly situated in a parallel plane to the sample surface, the basal plane. More advanced measurements and calculations of the spatial orientation, further explained in Supplement 1, support that the emitters polarization is almost in parallel to the basal plane, which are the orthogonal planes to the c-axis, indicated in Fig. 1(a).

We next studied the maximum emission rates of E_1 and E_3 with optimized excitation polarization. Fig. 3(d) shows the saturation behavior of both emitters and the associated background based on second-order autocorrelation histograms. The $g^2(0)$ based background
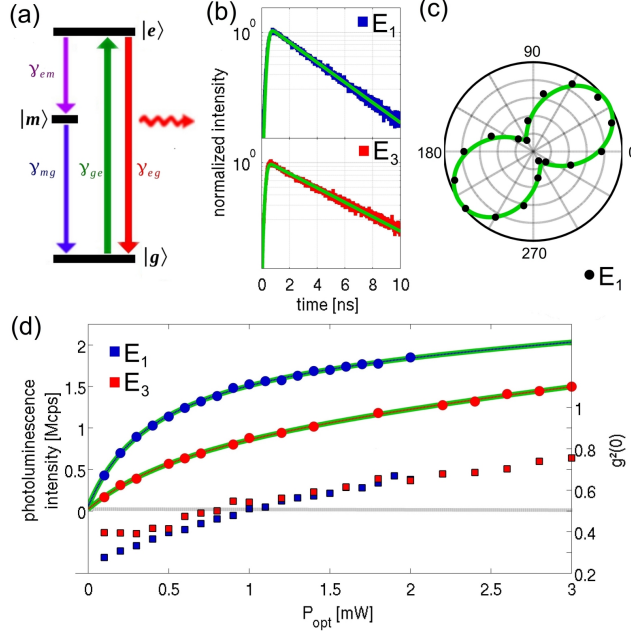
FIG. 3. (a) Jablonski diagram of a 3-level system with ground state ($|g\rangle$), excited state ($|e\rangle$), and metastable state ($|m\rangle$). (b) Lifetime measurements fitted with a single exponential decay function. (c) Polar plot of PL as a function of excitation laser polarization. (d) PL intensity measurements of the emitters evaluated at discrete excitation power to achieve maximal emission, fitted with Eq. 3 (green). Blue and red squares: acquired background during PL measurement based on second order autocorrelation histograms with corresponding axis on the right hand side. Both emitters show $g^2(0) < 0.5$ up to an excitation power of 1 mW.

measurements reveal single photon characteristics for both emitters up to excitation powers of 1 mW. To optimize the photon collection efficiency, these measurements were performed on a different confocal setup (Nikon, oil immersion, 1.3 NA, dichroic filter with cut-off wavelength of 552 nm, 560 nm longpass filter). The emission was equally distributed between two APDs to avoid saturation of the detectors.

Eq. 3, describing the measured power-dependent (P_{opt}) emission count rate (R_{FIT}), is the common function for 3-level systems to fit the power-dependent intensity measurements plotted in Fig. 3(d). The equation consists of collection and excitation efficiency parameters, η_{EX} respectively η_{COL}, a linear power dependent background slope (α), and a constant parameter for dark counts (β).

8

$$R_{FIT}(P_{opt}) = \frac{\eta_{COL}R_{INF}P_{opt}}{\eta_{EX}P_{SAT} + P_{opt}} + \alpha P_{opt} + \beta. \tag{3}$$

As seen in Fig. 3(d) the emitters exhibit high brightness with more than one million cps detected on each APD. The calculated saturation counts and corresponding power of E_1 are estimated to be at 1.942×10^6 cps and 0.425 mW and 1.154 million cps and 0.78 mW for E_3. To our knowledge, these are the brightest emitters in any bulk material reported to date, and among the brightest SPEs even if compared to color centers in diamond nanocrystals [27, 28]. Furthermore, these emitters are an order of magnitude brighter than a standard single NV center in a bulk diamond and comparable to a NV center enhanced via an optical nanostructure [29]. By extrapolation the determined count rates for collection efficiency enhancing nanostructures [30], we estimate single photon count rates of about 20×10^6 cps.

Photoluminescence at Cryogenic Temperatures

We performed low-temperature (18 K sample temperature) PL measurements in a closed-cycle Janis cryostat to study phonon coupling characteristics.

Fig. 4(a) shows low-temperature PL spectra of the three introduced emitters in Fig. 1(c). Common to all low temperature spectra is a strong peak which we attribute to the zero phonon line (ZPL) and a red shifted (~ 8 nm) phonon broadened peak indicated in the magnified cut out in Fig. 4(a). The ZPL emission wavelengths are illustrated in 4(b) as a histogram and reveal a spread from $\sim 575 - 610$ nm. There is no recognizable dependence between ZPL and polarization state.

Temperature dependent ZPL linewidth broadening reveals information about the dephasing mechanisms of the emitters, as well as the influence of the host crystal on the defects. Fig. 4(c) shows the temperature dependence of the emitter linewidth of the most dominant peak of E_1 at 581.4 nm approximated with Lorentzian fit functions. At 18 K we determine a linewidth of 0.095 $\pm$0.05 nm, not limited by the spectrometer resolution (< 0.1 nm). The lines were stable over the measurement period, and no diffusion or blinking on the ms time scale was observed. The linewidth broadening with increasing temperature fits very well with a T^3 function, similar to the silicon vacancy and other defects in diamond [28]. This is significantly different from the T^5 dependence of the NV color center in diamond that originates from the dynamic Jahn-Teller effect [31].
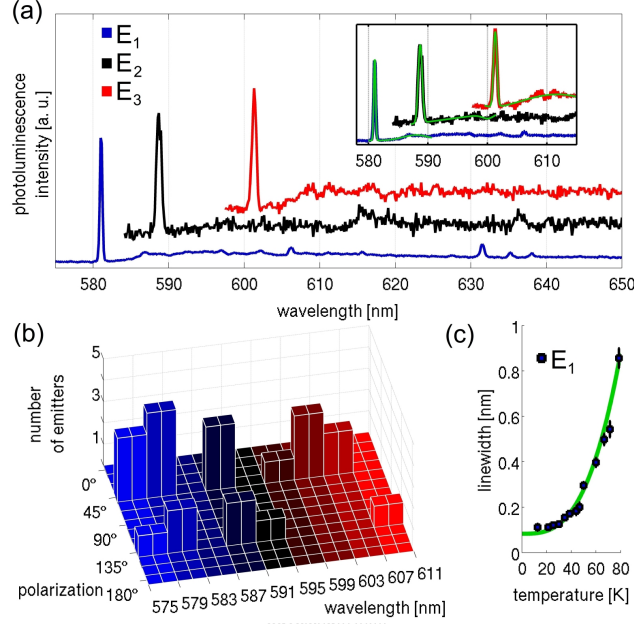
FIG. 4. (a) PL spectrum of E_1 (blue), E_2 (black), and E_3 (red) in an environment of 18 K. Inset, magnified spectral range containing ZPL (E_1: 581.2 nm, E_2: 588.9 nm, E_3: 601.5 nm) and first phonon modes, highlighted with green Gaussian fits. (b) Histogram of ZPLs with corresponding polarization of various room-temperature emitters at different wavelength recorded at cryogenic temperatures. (c) The linewidth broadening with increasing temperature of the dominant peak at 581.4 nm (E_1, blue squares) shows a T^3 (green) trend.

The population of the phonon side band (PSB), expressed in Eq. 4 by the Debye-Waller factor (DWF), can be estimated with the ratio of the ZPL PL emission, I_{ZPL}, relative to the total PL emission, $I_{TOT} = I_{ZPL} + I_{PSB}$, the combination of the ZPL PL emission with the phonon broadened PL, I_{PSB}. The DWF is calculated by separately fitting the zero phonon line and phonon side band (PSB) peaks with Lorentzian fit functions (Igor Pro™ 6.36).

$$DWF = \frac{I_{ZPL}}{I_{TOT}}. \tag{4}$$

At cryogenic temperatures we determine for E_1 a DWF of 33 $\pm$ 1 %. NV color centers yield a DWF of only about 3 % [22] but the silicon-vacancy center in diamonds has a DWF of more than 70 % [32]. A higher DWF is preferential to achieve better single photon emission characteristics [33] and could be directly enhanced via coupling to an optical cavity

[30].

DISCUSSION

Finally, we discuss the origin of these emitters. We attribute the investigated SPEs to the same emitter type due to similar low- and room-temperature PL spectra, the linear polarization data, and the matching of a 3-level system as the underlying model. We denote the emitter type as intrinsic due to the high density of emitters in high-purity SiC. Furthermore, the SPEs are observed in both electron irradiated and un-irradiated, annealed samples, with a higher density after electron irradiation.

To find a possible origin of the emitter, three major indicators are considered: (1) The investigated SPEs spectral components are in the red visible range. (2) To create photostable SPEs, it is necessary to anneal the SiC samples in an inert environment of at least $600°$ C. There is no observation of degradation regarding photostability or changes in emitter density up to annealing temperatures of at least $900°$ C. (3) There are two linear polarization states.

In the red visible spectral range, two SPEs in 4H-SiC are known and have been characterized, the carbon antisite-vacancy pair, characterized by Castelletto et al. [14], and a so far unknown emitter type, reported by Lohrmann et al. [34], presumably hosted by 6H-SiC inclusions. The carbon antisite-vacancy pair differs from the measured results especially by a red-shifted first ZPL (648.5 nm), a shorter excited state lifetime, and a stronger irradiation-density dependence. In contrast to the described SPE, the latter, yet unidentified emitter type exists in three different linear polarization states ($\phi_1 = 30°$, $\phi_2 = 90°$, $\phi_3 = 150°$) instead of two. Furthermore, its ZPLs are distributed over a broader spectrum ($\sim 550 - 750$ nm) and the saturated PL intensity is significantly smaller.

We exclude, as possible underlying defect structures, single carbon (C) and silicon (Si) vacancies, since the C vacancies tend to anneal out at temperatures above $500°$ C [35] and the Si vacancies [8, 15, 16] are in the NIR. The D_I-defect [36], D_{II}-defect [37], and di-vacancies [17] show optical signatures in different spectral ranges which eliminates them as possible emitter origins. Antisites, which are replaced Si (C) atoms by C (Si) atoms, show very low formation energies, hence, they are the most common defects in SiC [38]. Nevertheless, annealing temperatures around $\sim 200 - 300°$ C cause antisites to become mobile and they eventually recombine. In conclusion, none of the yet optically characterized emitters or

11

described defect structures in 4H-SiC seems to match the observed and measured features of the emitter.

Based on the conflict between the possible polarization states in hexagonal polytype hosts (60° separation between states, apparent in Fig. 1(a)) and the two observed orthogonal polarization states of the emitter, we propose a polytype inclusion. In the case of 3C-SiC just a single plane needs to be skipped and the violation in terms of the polarization is resolved [39]. During the production of SiC wafers by Cree inc. epitaxy defects such as 3C inclusions can be incorporated, in particular where the step-flow was interrupted during epitaxy layer growth [40].

CONCLUSION

We described an exceptionally bright, visible-spectrum single photon emitter in silicon carbide. The emitters exhibit count rates up to 2×10^6 cps at saturation at room-temperature — making them the brightest source of single photons from unpatterned bulk material. The emitters are abundant in a non-irradiated, annealed high purity 4H-SiC sample. Furthermore, their full polarization, narrow linewidth, and stability under constant laser excitation are promising attributes for applications in integrated nanophotonic technologies.

ACKNOWLEDGMENTS

---

* blienhar@mit.edu

[1] A. Migdall, S. c. Polyakov, J. Fan, and J. C. Bienfang, *Single-Photon Generation and Detection* (2013).

[2] C. Santori, D. Fattal, and Y. Yamamoto, *Single-photon Devices and Applications* (2010).

[3] B. Lounis and M. Orrit, Reports on Progress in Physics **68**, 1129 (2005).

[4] I. Aharonovich and E. Neu, Advanced Optical Materials **2**, 911 (2014).

[5] A. J. Morfa, B. C. Gibson, M. Karg, T. J. Karle, A. D. Greentree, P. Mulvaney, , and S. Tomljenovic-Hanic, Nano Letters **12**, 949 (2012).

[6] R. Kolesov, K. Xia, R. Reuter, R. Sthr, A. Zappe, J. Meijer, P. R. Hemmer, and J. Wrachtrup, Nature Communications **3** (2012), 10.1038/ncomms2034.

[7] B. Naydenov and F. Jelezko, *Single-Color Centers in Diamond as Single-Photon Sources and Quantum Sensors*, Vol. 15 (2015) pp. 303–318.

[8] V. A. Soltamov, A. A. Soltamova, P. G. Baranov, and I. I. Proskuryakov, Physical Review Letters **108** (2012), 10.1103/PhysRevLett.108.226402.

[9] J. R. Weber, W. F. Koehl, J. B. Varley, A. Janotti, B. B. Buckley, C. G. V. de Walle, and D. D. Awschalom, Proceedings of the National Academy of Sciences **107**, 8513 (2010).

[10] L. Childress, R. Walsworth, and M. Lukin, Physics Today **67**, 38 (2014).

[11] M. W. Doherty, N. B. Manson, P. Delaney, F. Jelezko, J. Wrachtrup, and L. C. Hollenberg, Physics Reports **528**, 1 (2013).

[12] J. B. Casady and R. W. Johnson, Solid-State Electronics **39**, 1409 (1996).

[13] D. Nakamura, I. Gunjishima, S. Yamaguchi, T. Ito, A. Okamoto, H. Kondo, S. Onda, and K. Takatori, Nature **430**, 1009 (2004).

[14] S. Castelletto, B. C. Johnson, V. Ivdy, N. Stavrias, T. Umeda, A. Gali, and T. Ohshima, Nature Materials **13**, 151 (2014).

[15] P. G. Baranov, A. P. Bundakova, I. V. Borovykh, S. B. Orlinskii, R. Zondervan, and J. Schmidt, Jounal of Experimental and Theoretical Physics Letters **86**, 202 (2007).

[16] H. Kraus, V. A. Soltamov, D. Riedel, S. Vth, F. Fuchs, A. Sperlich, P. G. Baranov, V. Dyakonov, and G. V. Astakhov, Nature Physics **10**, 157 (2014).

[17] V. S. Vainer and V. Il'in, Soviet Physics Solid State **23**, 2126 (1981).

[18] W. F. Koehl, B. B. Buckley, F. J. Heremans, G. Calusine, and D. D. Awschalom, Nature **479**, 84 (2011).

[19] D. J. Christle, Nature Materials **14** (2015).

[20] P. T. B. Shaffer, Applied Optics **10**, 1034 (1971).

[21] J. C. Burton, L. Sun, F. H. Long, Z. C. Feng, and I. T. Ferguson, Physical Review B **59**, 7282 (1999).

[22] N. B. Manson, J. P. Harrison, and M. J. Sellars, Physical Review B **74**, 104303 (2006).

[23] R. Loudon, *The Quantum Theory of Light* (1983).

[24] S. C. Kitson, P. Jonsson, J. G. Rarity, and P. R. Tapster, Physical Review A **58**, 620 (1998).

[25] M. Berthel, O. Mollet, G. Dantelle, T. Gacoin, S. Huant, and A. Drezet, Physical Review B **91**, 035308 (2015).

[26] I. Aharonovich, Physical Review B **81** (2010).

[27] I. Aharonovich, S. Castelletto, D. A. Simpson, A. Stacey, J. McCallum, A. D. Greentree, and S. Prawer, Nano Letters **9**, 3191 (2009).

[28] E. Neu, Optics Express **20**, 19956 (2012).

[29] S. Schietinger, M. Barth, T. Aichele, and O. Benson, Nano Letters **9**, 1694 (2009).

[30] L. Li, E. H. Chen, J. Zheng, S. L. Mouradian, F. Dolde, T. Schrder, S. Karaveli, M. L. Markham, D. J. Twitchen, and D. Englund, Nano Letters **15**, 1493 (2015).

[31] K.-M. C. Fu, C. Santori, P. E. Barclay, L. J. Rogers, N. B. Manson, and R. G. Beausoleil, Physical Review Letters **103**, 256404 (2009).

[32] S. Pezzagna, D. Rogalla, D. Wildanger, J. Meijer, and A. Zaitsev, New Journal of Physics **13**, 035024 (2011).

[33] A. D. Greentree, B. A. Fairchild, F. M. Hossain, and S. Prawer, Materials Today **11**, 22 (2008).

[34] A. Lohrmann, N. Iwamoto, Z. Bodrog, S. Castelletto, T. Ohshima, T. Karle, A. Gali, S. Prawer, J. McCallum, and B. Johnson, Nature Communications **6**, 7783 (2015).

[35] M. Y. Um, I. S. Jeon, D. I. Eom, and H. J. Kim, Japanese Journal of Applied Physics **43**, 4114 (2004).

[36] C. Haberstroh, R. Helbig, and R. A. Stein, Journal of Applied Phyiscs **509**, 76 (1994).

[37] F. Carlsson, Materials Science Forum **433-436**, 345 (2003).

[38] L. Torpo, S. Pykk, and R. M. Nieminen, Physical Review B **57**, 6243 (1998).

[39] S. Bai, R. P. Devatyand, W. J. Choyke, U. Kaiser, G. Wagner, and M. F. MacMillan, Applied Physics Letter **83**, 3171 (2003).

[40] "Cree silicon carbide substrates and epitaxy," (2013), http://www.cree.com/~/media/ Files/Cree/Chips-and-Material/Data-Sheets-Material/MATCATALOG.pdf.